Editors' Suggestion

Realization of the Axion Insulator State in Quantum Anomalous Hall Sandwich Heterostructures

Di Xiao,[1] Jue Jiang,[1] Jae-Ho Shin,[1] Wenbo Wang,[2] Fei Wang,[1] Yi-Fan Zhao,[1] Chaoxing Liu,[1] Weida Wu,[2] Moses H. W. Chan,[1,*] Nitin Samarth,[1,†] and Cui-Zu Chang[1,‡]

[1]*Department of Physics, Pennsylvania State University, University Park, Pennsylvania 16802, USA*
[2]*Department of Physics and Astronomy, Rutgers University, Piscataway, New Jersey 08854, USA*

(Received 1 October 2017; revised manuscript received 28 November 2017; published 31 January 2018)

The "magnetoelectric effect" arises from the coupling between magnetic and electric properties in materials. The Z_2 invariant of topological insulators (TIs) leads to a quantized version of this phenomenon, known as the topological magnetoelectric (TME) effect. This effect can be realized in a new topological phase called an "axion insulator" whose surface states are all gapped but the interior still obeys time reversal symmetry. We demonstrate such a phase using electrical transport measurements in a quantum anomalous Hall (QAH) sandwich heterostructure, in which two compositionally different magnetic TI layers are separated by an undoped TI layer. Magnetic force microscopy images of the same sample reveal sequential magnetization reversals of the top and bottom layers at different coercive fields, a consequence of the weak interlayer exchange coupling due to the spacer. When the magnetization is antiparallel, both the Hall resistance and Hall conductance show zero plateaus, accompanied by a large longitudinal resistance and vanishing longitudinal conductance, indicating the realization of an axion insulator state. Our findings thus show evidence for a phase of matter distinct from the established QAH state and provide a promising platform for the realization of the TME effect.

DOI: 10.1103/PhysRevLett.120.056801

Three-dimensional (3D) topological insulators (TIs) are unusual quantum materials that host conducting helical Dirac states on their surfaces, which are protected by time reversal symmetry (TRS), but are electrically insulating in the bulk [1,2]. TI is distinct from a trivial insulator by its unique electromagnetic response, described by the so-called θ term shown below, in addition to the ordinary Maxwell terms [3–6].

$$S_\theta = \frac{\theta}{2\pi}\frac{e^2}{h}\int d^3x dt \vec{E}\cdot\vec{B}.$$

Here $\vec{E}$ and $\vec{B}$ are the conventional electric and magnetic fields inside an insulator, e is electron charge, and θ is the dimensionless pseudoscalar parameter describing the insulator. For a trivial insulator, $\theta = 0$, while for a TI, $\theta = \pi$. When TRS is preserved, θ is either 0 or π, reflecting its topological nature. This θ term is related to the axion electrodynamics in particle physics [7]. Since the $\vec{E}\cdot\vec{B}$ term can be rewritten as a total derivative, its effect manifests on the surface states. A half-integer quantum Hall effect on the TI surface occurs once the surface Dirac fermions acquire a mass; i.e., the surface state is gapped by magnetism. Such a half-integer quantum Hall effect on the TI surface can lead to a variety of exotic phenomena such as the quantum anomalous Hall (QAH) effect [3,8–15], the quantized magneto-optical effect [3,16,17], the topological magnetoelectric (TME) effect [3–6,18], and the image magnetic monopole [19]. The QAH and quantized magneto-optical effects have been experimentally demonstrated in pure or magnetic TI films [10–13,20–22]. The TME effect refers to the quantized response of electric polarization to applied magnetic fields and vice versa. The realization of the TME effect requires the following three conditions: (i) the TI film should be in the 3D regime; (ii) all the surfaces are gapped with the chemical potential lying within the gaps; (iii) the interior of the TI maintains TRS or inversion symmetry to maintain $\theta = \pi$ in the bulk. A material system allowing for the realization of the TME effect is known as an axion insulator [3–5].

Recently, two papers reported the possible realization of the axion insulator. Mogi *et al.* [23] fabricated asymmetric $(Bi,Sb)_2Te_3$ multilayer heterostructures with Cr modulation doping. The observation of a zero Hall conductance (σ_{xy}) plateau was interpreted as evidence of an axion insulator due to antiparallel magnetization alignment of the top and bottom Cr-doped $(Bi,Sb)_2Te_3$ layers. Subsequent magnetic domain imaging measurements on the same sample, however, failed to find evidence of antiparallel magnetization alignment at any external magnetic field ($\mu_0 H$) [24]. It is likely that the reported zero σ_{xy} plateau is not a result of antiparallel magnetization alignment but an artifact due to the conversion of the measured longitudinal resistance (ρ_{xx}) and Hall resistance (ρ_{yx}) into σ_{xy}, i.e., $\sigma_{xy} = [(\rho_{yx})/(\rho_{xx}^2 + \rho_{yx}^2)]$. A nearly zero σ_{xy}

plateau can arise because of the large ρ_{xx} ($\sim 40h/e^2$) at the coercive field (H_c), as shown in Fig. S3h of Ref. [23]. If the top and bottom Cr-doped TI layers indeed possess antiparallel magnetization alignment in the Cr modulation doped QAH samples, then a zero ρ_{yx} plateau should be present, but this is absent in Ref. [23]. Grauer *et al.* [25] also claimed the observation of an "axion insulator" in a uniformly doped QAH sample in the 3D regime. However, the presence of the 1D chiral edge mode of the 3D QAH state implies that side surfaces are not gapped, thus violating the condition (ii) noted above. In addition, the magnetic moments are evenly distributed in the uniformly doped QAH samples, so the interior of the uniformly doped samples no longer maintains TRS, violating condition (iii). We therefore suggest that there is as yet no clear experimental evidence of an axion insulator that satisfies all the necessary criteria as outlined above.

A 3D FM-TI-FM QAH sandwich heterostructure has been proposed for realizing the axion insulator state in antiparallel magnetization alignment [3–5]. It has been shown that magnetically doped TI layers can be epitaxially grown on an undoped TI layer and vice versa to form the required FM-TI-FM sandwich heterostructures [23,26,27]. If the top and bottom $(Bi, Sb)_2Te_3$ layers are doped with two different magnetic ions, specifically, Cr- and V-, and the interlayer coupling exchange field (H_E) is substantially smaller than the difference ΔH_c between the H_cs of the two magnetic layers, an antiparallel magnetization alignment may appear when the external H lies between two H_cs. This is the case since the H_cs of the Cr- and V-doped QAH films [10,13] are respectively ~0.15 T and ~1 T, as shown in Fig. 1(a).

In this *Letter*, we report observations that satisfy the three necessary conditions outlined above for an axion insulator state in V-doped $(Bi, Sb)_2Te_3$/$(Bi, Sb)_2Te_3$/Cr-doped $(Bi, Sb)_2Te_3$ sandwich heterostructures. Electrical transport and magnetic force microscopy (MFM) measurements show zero σ_{xy} and also ρ_{yx} plateaus in the antiparallel magnetization alignment configuration of the top and bottom magnetic TI layers, demonstrating the realization of an axion insulator state. The axion insulator state appears when the H lies between two H_cs of the top and bottom magnetic layers.

The V-doped $(Bi, Sb)_2Te_3$/$(Bi, Sb)_2Te_3$/Cr-doped $(Bi, Sb)_2Te_3$ QAH sandwich heterostructures are grown on $SrTiO_3(111)$ substrate in a molecular beam epitaxy (MBE) chamber. As shown in Fig. 1(b), the bottom magnetic layer is 3 quintuple layers (QL) Cr-doped $(Bi, Sb)_2Te_3$, and the top magnetic layer is 3QL V-doped $(Bi, Sb)_2Te_3$. The undoped $(Bi, Sb)_2Te_3$ films separating two magnetic layers have thicknesses of 4, 5, and 6 QL. These relatively thick spacer films are chosen to reduce H_E and prevent the hybridization of the top and bottom surface states [25,28–30]. In our experiment, the three different thicknesses of the TI spacer show very similar results, suggesting that a spacer of 4 QL is already sufficient in

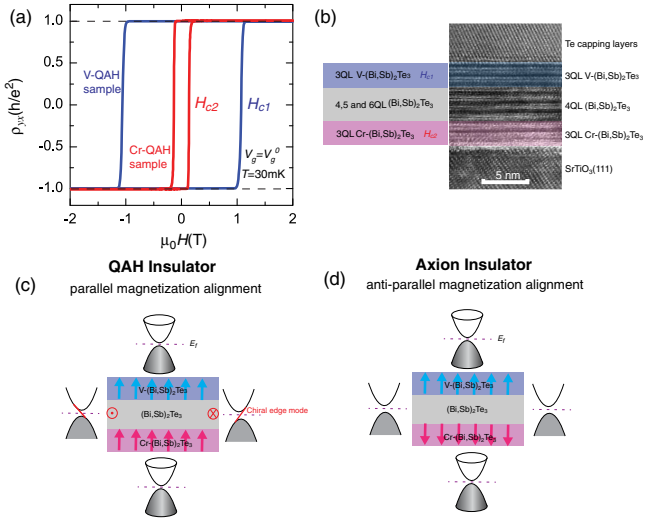

FIG. 1. V-doped $(Bi, Sb)_2Te_3$/TI/Cr-doped $(Bi, Sb)_2Te_3$ sandwich heterostructure. (a) Signatures of the QAH insulator states in individual Cr- and V-doped $(Bi, Sb)_2Te_3$ films measured at $T = 30$ mK. The H_c of the V-doped QAH film $H_{c1} \sim 1.06$ T; the H_c of the Cr-doped QAH film $H_{c2} \sim 0.14$ T. (b) Schematic drawing and cross-sectional TEM image of a QAH sandwich heterostructure. (c) Schematics of a sandwich heterostructure with parallel magnetization alignment surfaces, supporting a 1D chiral edge state. (d) Schematics of a sandwich heterostructure with antiparallel magnetization alignment surfaces, supporting an axion insulator state.

weakening the H_E (see detailed comparisons in the Supplemental Material [31]). In this Letter, we focus on two sandwich heterostructures with a spacer of 5 QL (referred to as 3-5-3 SH1 and SH2) from the same sample wafer. The samples are scratched into Hall bar geometry ($\sim 1.0 \times 0.5$ mm). A physical property measurement system (PPMS) cryostat is used to initially screen the samples, the principal transport results shown here are then carried out in a dilution refrigerator (Leiden Cryogenics, 10 mK, 9T). The MFM experiments are carried out in a homemade cryogenic atomic force microscope with *in situ* transport measurements.

By carefully tuning the Bi/Sb ratio in each layer of the 3-5-3 sandwich heterostructure, we locate the chemical potential close to its charge neutral point (V_g^0). The high dielectric constant of the $SrTiO_3$ substrate at low temperature allows us to fine tune by electric gating the chemical potential within the exchange gap on the top and bottom surfaces. When the magnetization of the top V-doped $(Bi, Sb)_2Te_3$ layer is parallel to that of the bottom Cr-doped $(Bi, Sb)_2Te_3$ layer, the 3-5-3 sandwich heterostructure exhibits a QAH state with a 1D chiral edge mode flowing along the edge of the sandwich sample, as shown in Fig. 1(c). Since H_c of the Cr-doped $(Bi, Sb)_2Te_3$ layer is much smaller than that of the V-doped $(Bi, Sb)_2Te_3$ layer [Fig. 1(a)], sweeping the external $\mu_0 H$ first reverses the magnetization of the Cr-doped $(Bi, Sb)_2Te_3$ layer. Because of the weak H_E between the top and bottom magnetic

layers, the V-doped $(Bi, Sb)_2Te_3$ layer will remain in its initial magnetization state until the external H reaches $-H_{c1}$. Therefore, when $-H_{c1} < H < -H_{c2}$, the magnetizations of two magnetic layers are in antiparallel alignment. In this case, the top and bottom surfaces can be considered to be in half-integer "QAH states" with $\sigma^t_{xy} = 0.5e^2/h$ and $\sigma^b_{xy} = -0.5e^2/h$, yielding zero σ_{xy} plateau and eliminating the 1D chiral edge state. Provided the quantum confinement effect gaps the side surface states, the sandwich structure in antiparallel magnetization alignment regions will satisfy all the conditions for the axion insulator state as illustrated in Fig. 1(d).

Figures 2(a) and 2(b) show the $\mu_0 H$ dependence of the longitudinal conductance (σ_{xx}) and σ_{xy} of the 3-5-3 SH1 measured at $T = 30$ mK and $V_g = V_g^0 = +18$ V. The red and blue curves represent downward and upward $\mu_0 H$ sweeps, respectively. At $\pm H_c$s ($\pm H_{c1}$ for the top V-doped TI layer and $\pm H_{c2}$ for the bottom Cr-doped TI layer), we observe sharp peaks of σ_{xx} [Fig. 2(a)]. Correspondingly, the $\mu_0 H$ dependence of σ_{xy} shows a two-step transition from e^2/h to 0 and then $-e^2/h$ or from $-e^2/h$ to 0 and then e^2/h. Zero σ_{xy} plateaus are observed in the intermediate field ranges $-H_{c1} < H < -H_{c2}$ and $H_{c2} < H < H_{c1}$. We noted that zero σ_{xy} plateau has been observed in uniformly doped QAH samples, where it is attributed to large ρ_{xx} resulting from scattering due to the random magnetic domains at H_c [36–38]. In contrast, the zero σ_{xy} plateau observed here, as we will show below, results from the cancellation of the top and bottom surface conduction in the antiparallel magnetization alignment, consistent with an axion insulator. In order to demonstrate the antiparallel magnetization alignment in the zero σ_{xy} plateau regions, we carried out MFM measurements.

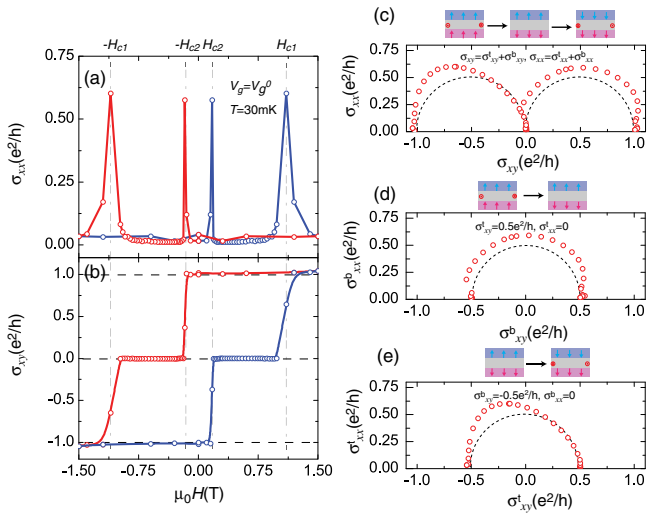

FIG. 2. Signature of an axion insulator in a 3-5-3 SH1 with antiparallel magnetization alignment. (a, b) $\mu_0 H$ dependence of σ_{xx} and σ_{xy} of 3-5-3 SH1 at $V_g = V_g^0$ and $T = 30$ mK. An axion insulator is observed if the zero σ_{xy} plateau region is the consequence of antiparallel magnetization alignment. The red and blue lines are guides to the eye. (c) Flow diagram of (σ_{xy}, σ_{xx}) of the 3-5-3 SH1 from $\mu_0 H = 1.8$ to $\mu_0 H = -1.8$ T [the red curves in (a) and (b)]. Two semicircles of radius 0.5 h/e^2 centered at ($0.5h/e^2$, 0) and ($-0.5h/e^2$, 0) are shown in dashed lines. (d) Flow diagram of (σ^b_{xy}, σ^b_{xx}) of the bottom surface from $\mu_0 H = 1.8$ to $\mu_0 H = -0.45$ T. (e) Flow diagram of (σ^t_{xy}, σ^t_{xx}) of the top surface from $\mu_0 H = -0.45$ to $\mu_0 H = -1.8$ T. A semicircle of radius $0.5h/e^2$ centered at (0, 0) is shown in a dashed line in (d) and (e). Here $\mu_0 H = -0.45$ T is chosen to separately study the scalings of the top and bottom surfaces of the QAH sandwich heterostructures in proper magnetic field sweeping regions.

Figures 3(a)–3(j) show *in situ* ρ_{yx} and MFM images at various $\mu_0 H$s on the 3-5-3 SH2 at $T = 5.3$ K and $V_g = 0$ V. The ρ_{yx} shows a two-step transition, similar to the zero ρ_{yx} plateau at $T = 30$ mK and $V_g = V_g^0$ [Figs. 3(k) and 3(m)]. We note that the zero ρ_{yx} plateau is absent in either uniformly doped or the Cr modulation doped QAH samples [23,26,36,37]. The 3-5-3 SH2 was magnetically trained first by an upward sweep up to $\mu_0 H = 1.5$ T before being swept downward. When $\mu_0 H = -0.01$ T, the MFM contrast is uniform (red), indicating that both top V- and bottom Cr-doped TI layers have upward magnetization [Fig. 3(c)]. At $\mu_0 H = -0.05$ T, some reversed magnetic domains [green regions in Fig. 3(d)] appear, presumably in the "softer" Cr-doped TI layer. As $\mu_0 H$ is swept further, the green regions expand and fill up the whole scan area at $\mu_0 H = -0.09$ T, indicating the uniform antiparallel magnetization alignment over the entire 3-5-3 SH2. When $\mu_0 H$ is further swept toward H_{c1}, new reversed magnetic domains [blue regions in

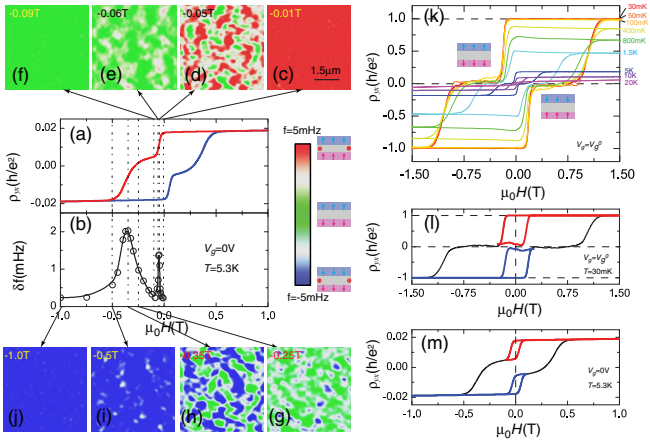

FIG. 3. Two-step magnetization reversal in the 3-5-3 SH2. (a) $\mu_0 H$ dependence of ρ_{xy} of 3-5-3 SH2 at $V_g = 0$ V and $T = 5.3$ K. (b) $\mu_0 H$ dependence of magnetic domain contrasts (δf) at $V_g = 0$ and $T = 5.3$ K. The δf is estimated from the rms value of MFM images in (c)–(j). (c)–(j)The MFM images at various $\mu_0 H$s. Red and blue represent respectively upward and downward parallel magnetization alignment regions, green represents antiparallel magnetization alignment regions. The Hall traces in (a) and the MFM images in (c)–(j)are measured simultaneously. (k) $\mu_0 H$ dependence of ρ_{yx} at various temperatures. ρ_{yx} exhibits two-step transition when $T < 10$ K. (l), (m) Minor loops of the ρ_{yx} at $V_g = V_g^0$ and $T = 30$ mK (l) and at $V_g = 0$ V, and $T = 5.3$ K (m).

Fig. 3(g)] nucleate at different locations, presumably in the "harder" V-doped TI layer. Downward parallel magnetization alignment regions (blue) expand at the cost of antiparallel magnetization alignment regions (green) [Figs. 3(g) and 3(h)]. When $\mu_0 H = -1.0$ T, the MFM image is uniformly blue, indicating a uniform downward parallel magnetization alignment [Fig. 3(j)]. The direct observation of magnetic domains also allows us to extract the H_cs of magnetic layers. For our sandwich heterostructure, the $\mu_0 H$ dependence of the magnetic domain contrast (δf), estimated from the root-mean-square (rms) value of the MFM signal shows two peaks when the parallel and antiparallel magnetization alignment regions are equally populated [Fig. 3(b)]. These two peaks correspond to the H_cs of top and bottom magnetic TI layers, in excellent agreement with those extracted from ρ_{yx} shown in Fig. 3(a). Our MFM measurements therefore demonstrated the presence of antiparallel magnetization alignment region (i.e. $-H_{c1} < H < -H_{c2}$) at 5.3 K. It is reasonable to expect such behavior to persist to lower temperatures that bring out the QAH state.

Figure 3(k) shows the $\mu_0 H$ dependence of ρ_{yx} of 3-5-3 SH2 over the temperature range 30 mK $< T <$ 20 K (see Fig. S9b in the Supplemental Material [31] for σ_{xy}). Both ρ_{yx} and σ_{xy} exhibit a two-step transition feature up to $T = 10$ K. The two-step feature sharpens with decreasing temperature showing zero ρ_{yx} and σ_{xy} plateaus for $T < 1.5$ K. To confirm the antiparallel magnetization alignment in zero ρ_{yx} and σ_{xy} plateau regions at $T = 30$ mK, we compared the minor loops at $T =$ 30 mK with $V_g = V_g^0$ and $T = 5.3$ K with $V_g = 0$ V [Figs. 3(l) and 3(m)]. The H_E can be estimated by $H_E = (|H^L_{c,\mathrm{minor}} - H^R_{c,\mathrm{minor}}|/2)$, where $H^L_{c,\mathrm{minor}}$ and $H^R_{c,\mathrm{minor}}$ denote the left and right H_c of minor loops [39,40]. The H_Es at $T = 30$ mK and 5.3 K are ~115 and ~84 Oe, respectively. Since the H_cs of two magnetic TI layers are also functions of T, we define a relative H_E value $\alpha = [(H_E)/(H_{c1} - H_{c2})]$ to compare the interlayer coupling strengths at different Ts. We find that $\alpha \sim 0.013$ at $T = 30$ mK and ~0.028 at $T = 5.3$ K. With the MFM observation at 5.3 K, the smaller α at $T = 30$ mK confirms not surprisingly the robust antiparallel magnetization alignment in the zero ρ_{yx} and σ_{xy} plateau regions. Therefore, the axion insulator state is indeed realized in the zero ρ_{yx} and σ_{xy} plateau regions at $T = 30$ mK.

Flow diagram (σ_{xy}, σ_{xx}) of the 3-5-3 SH1 from $\mu_0 H =$ 1.8 to $\mu_0 H = -1.8$ T [the red curves in Figs. 2(a) and 2(b)] at $T = 30$ mK is shown in Fig. 2(c). Two circles of radius $0.5\, e^2/h$ centered at $(\sigma_{xy}, \sigma_{xx}) = (\pm 0.5e^2/h, 0)$ appear, the QAH state and the axion insulator state correspond to $(\sigma_{xy}, \sigma_{xx}) = (\pm e^2/h, 0)$ and (0, 0), respectively. The sequential magnetization reversals of the top and bottom layers allow separation of the scaling of $(\sigma_{xy}, \sigma_{xx})$ of the top and bottom surfaces. In the antiparallel magnetization alignment (axion insulator) regions, the top V-doped TI layer maintains upward magnetization. When $\mu_0 H$ is tuned from 1.8 to −0.45 T, the plateau transition around $-H_{c2} \sim -0.17$ T is induced by the magnetization reversal of the Cr-doped TI layer, and the top surface keeps $(\sigma^t_{xy}, \sigma^t_{xx}) = (+0.5e^2/h, 0)$. Thus, we acquire the bottom surface scaling of $(\sigma^b_{xy}, \sigma^b_{xx}) = (\sigma_{xy}, \sigma_{xx}) - (\sigma^t_{xy}, \sigma^t_{xx})$, as shown in Fig. 2(d), and a semicircle of radius $0.5e^2/h$ centered at (0,0) appears, consistent with the predicted flow diagram for a single surface state [3]. When $\mu_0 H$ is further tuned from −0.45 to −1.8 T, the bottom surface contributes $(\sigma^b_{xy}, \sigma^b_{xx}) = (-0.5e^2/h, 0)$, so the top surface scaling of $(\sigma^t_{xy}, \sigma^t_{xx}) = (\sigma_{xy}, \sigma_{xx}) - (\sigma^b_{xy}, \sigma^b_{xx})$ is revealed [Fig. 2(e)]. The same scaling behavior found at the top and bottom surfaces of the sandwich heterostructure confirms that each surface contributes half-integer quantization to the total σ_{xy}.

Figure 4 shows the $\mu_0 H$ dependence of ρ_{xx}, ρ_{yx}, and σ_{xy} of 3-5-3 SH1 at various V_gs at 30 mK. At $V_g = V_g^0 = +18$ V, in the parallel magnetization alignment region, we find the QAH state with $\rho_{xx} \sim 126\ \Omega$ and ρ_{yx} and σ_{xy} fully quantized. However, in the antiparallel magnetization alignment region, ρ_{xx} becomes very large (>1 MΩ) exceeding the range of our resistance bridge, and σ_{xy} shows a zero plateau, corresponding to the axion insulator state. Unlike the ρ_{yx} plateau in 3-5-3 SH2 [Figs. 3(k) and 3(l)], the ρ_{yx} of 3-5-3 SH1 shows substantial

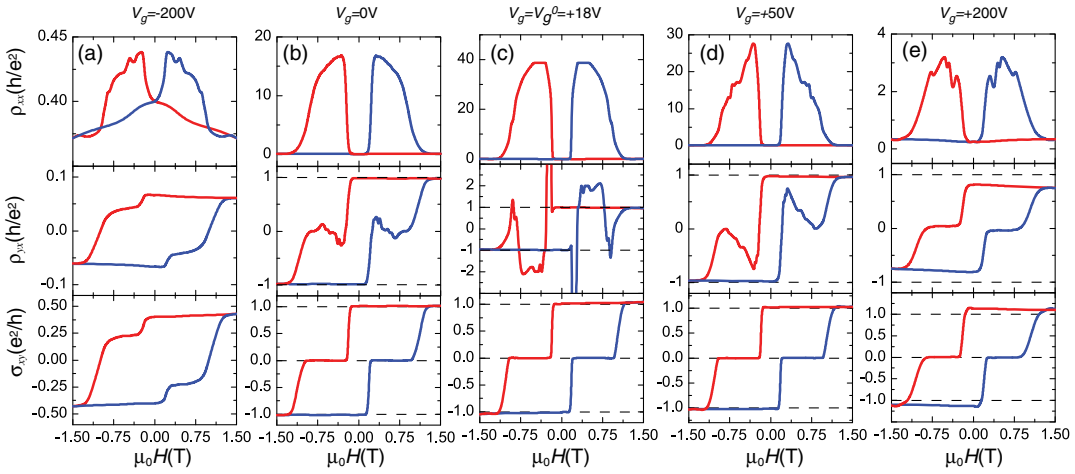

FIG. 4. Gate tuning of ρ_{xx}, ρ_{yx}, and σ_{xy} of the 3-5-3 SH1 at $T = 30$ mK. (a)–(e) $\mu_0 H$ dependence of ρ_{xx} (top panels), ρ_{yx} (middle panels), and σ_{xy} (bottom panels) at varied V_gs. The red and blue curves show results sweeping $\mu_0 H$ downward and upward, respectively.

fluctuations in the antiparallel magnetization alignment regions [see middle panels of Figs. 4(b)–4(d)]. This phenomenon is most likely due to the unavoidable electrical "pickup" in ρ_{yx} from the extremely large ρ_{xx} with our imperfect Hall bar geometry.

The large ρ_{xx} in antiparallel magnetization alignment confirms the insulating property of the axion insulator state. The top and bottom magnetic TI layers could be considered as a half-integer "QAH insulator" with $\sigma_{xy} = 0.5e^2/h$, but the 1D chiral edge mode of the entire sandwich heterostructure is forbidden due to their antiparallel magnetization alignment. Furthermore, the observed large ρ_{xx} also exclude the existence of helical side surface states in the sandwich heterostructure, reflecting the effect of quantum confinement. Since there is no conduction channel in the 3-5-3 sandwich heterostructure with antiparallel magnetization alignment, the axion insulator state is much more insulating than that induced by scattering from the multimagnetic domains in uniformly magnetically doped QAH samples [10–15,25,36,37]. Thus, the external $\mu_0 H$ can turn off or on the 1D chiral edge state in antiparallel and parallel magnetization alignment regions, leading to an "off or on" ratio of ~8000 for ρ_{xx}.

The QAH and axion insulator states persist when n-type carriers are introduced [Figs. 4(c)–4(e)]. The ρ_{xx} in antiparallel magnetization alignment is tuned from $>40h/e^2$ at $V_g = V_g^0$ to $\sim 3h/e^2$ at $V_g = +200$ V, and the zero ρ_{yx} plateau becomes more obvious, as shown in the middle panel of Fig. 4(e). When $V_g < 0$ V, ρ_{xx}, ρ_{yx}, and σ_{xy} are significantly altered, and their values become very small [Fig. 4(a)], indicating that the chemical potential of the sandwich heterostructure has crossed the bulk valence bands. In this case, the FM order is modulated by the Ruderman-Kittel-Kasuya-Yosida interaction [41], rather than the van Vleck interaction when the chemical potential is located in the vicinity of $V_g = V_g^0$ [8].

To summarize, our transport studies, complemented by MFM measurements, demonstrated the axion insulator state in the antiparallel magnetization alignment of the top and bottom magnetic layers of the QAH sandwich heterostructures. By separately analyzing the scaling of the transitions of the top and bottom magnetic layers, we show clearly that each surface of the QAH insulator or axion insulator contributes half-integer quantization. The demonstration of the axion insulator state in QAH sandwich heterostructures paves the way for the experimental exploration of the TME effect and other fascinating topological phenomena.

The authors would like to thank K. F. Mak, A. H. MacDonald, and B. H. Yan for the helpful discussions and A. Richardella, T. Pillsbury, J. Kally, W. Zhao, Z. Chen, H. L. Fu, X. Lin, S. Jiang, and S. Kempinger for help with experiments. D. X., J. J., F. W., Y. Z., C. L., C. Z. C., and N. S. acknowledge support from the Penn State Two-Dimensional Crystal Consortium-Materials Innovation Platform (2DCC-MIP) under NSF Grant No. DMR-1539916. D. X. and N. S. also acknowledge support from Office of Naval Research (Grant No. N00014-15-1-2370) and from ARO MURI (W911NF-12-1-0461). J. H. S. and M. H. W. C. acknowledge the support from NSF Grant No. DMR-1707340. C. X. L acknowledges the support from Office of Naval Research (Grant No. N00014-15-1-2675). C. Z. C. acknowledges support from a startup grant provided by Penn State. Work at Rutgers was supported by the U.S. Department of Energy (DOE), Office of Science, Basic Energy Sciences (BES) under Award No. DE-SC0018153.

D. X. and J. J. contributed equally to this work.

Note added.—Recently, we became aware of similar work published in *Sci. Adv.* [42].

*Corresponding author.
mhc2@psu.edu
†Corresponding author.
nxs16@psu.edu
‡Corresponding author.
cxc955@psu.edu

[1] X. L. Qi and S. C. Zhang, Rev. Mod. Phys. **83**, 1057 (2011).
[2] M. Z. Hasan and C. L. Kane, Rev. Mod. Phys. **82**, 3045 (2010).
[3] X. L. Qi, T. L. Hughes, and S. C. Zhang, Phys. Rev. B **78**, 195424 (2008).
[4] J. Wang, B. Lian, X. L. Qi, and S. C. Zhang, Phys. Rev. B **92**, 081107 (2015).
[5] T. Morimoto, A. Furusaki, and N. Nagaosa, Phys. Rev. B **92**, 085113 (2015).
[6] A. M. Essin, J. E. Moore, and D. Vanderbilt, Phys. Rev. Lett. **102**, 146805 (2009).
[7] F. Wilczek, Phys. Rev. Lett. **58**, 1799 (1987).
[8] R. Yu, W. Zhang, H. J. Zhang, S. C. Zhang, X. Dai, and Z. Fang, Science **329**, 61 (2010).
[9] C. X. Liu, X. L. Qi, X. Dai, Z. Fang, and S. C. Zhang, Phys. Rev. Lett. **101**, 146802 (2008).
[10] C. Z. Chang *et al.*, Science **340**, 167 (2013).
[11] X. F. Kou, S. T. Guo, Y. B. Fan, L. Pan, M. R. Lang, Y. Jiang, Q. M. Shao, T. X. Nie, K. Murata, J. S. Tang, Y. Wang, L. He, T. K. Lee, W. L. Lee, and K. L. Wang, Phys. Rev. Lett. **113**, 137201 (2014).
[12] J. G. Checkelsky, R. Yoshimi, A. Tsukazaki, K. S. Takahashi, Y. Kozuka, J. Falson, M. Kawasaki, and Y. Tokura, Nat. Phys. **10**, 731 (2014).
[13] C. Z. Chang, W. W. Zhao, D. Y. Kim, H. J. Zhang, B. A. Assaf, D. Heiman, S. C. Zhang, C. X. Liu, M. H. W. Chan, and J. S. Moodera, Nat. Mater. **14**, 473 (2015).
[14] M. H. Liu, W. D. Wang, A. R. Richardella, A. Kandala, J. Li, A. Yazdani, N. Samarth, and N. P. Ong, Sci. Adv. **2**, e1600167 (2016).
[15] A. Kandala, A. Richardella, S. Kempinger, C. X. Liu, and N. Samarth, Nat. Commun. **6**, 7434 (2015).
[16] W. K. Tse and A. H. MacDonald, Phys. Rev. Lett. **105**, 057401 (2010).
[17] J. Maciejko, X. L. Qi, H. D. Drew, and S. C. Zhang, Phys. Rev. Lett. **105**, 166803 (2010).

[18] K. Nomura and N. Nagaosa, Phys. Rev. Lett. **106**, 166802 (2011).
[19] X. L. Qi, R. D. Li, J. D. Zang, and S. C. Zhang, Science **323**, 1184 (2009).
[20] L. Wu, M. Salehi, N. Koirala, J. Moon, S. Oh, and N. P. Armitage, Science **354**, 1124 (2016).
[21] V. Dziom, A. Shuvaev, A. Pimenov, G. V. Astakhov, C. Ames, K. Bendias, J. Bottcher, G. Tkachov, E. M. Hankiewicz, C. Brune, H. Buhmann, and L. W. Molenkamp, Nat. Commun. **8**, 15197 (2017).
[22] K. N. Okada, Y. Takahashi, M. Mogi, R. Yoshimi, A. Tsukazaki, K. S. Takahashi, N. Ogawa, M. Kawasaki, and Y. Tokura, Nat. Commun. **7**, 12245 (2016).
[23] M. Mogi, M. Kawamura, R. Yoshimi, A. Tsukazaki, Y. Kozuka, N. Shirakawa, K. S. Takahashi, M. Kawasaki, and Y. Tokura, Nat. Mater. **16**, 516 (2017).
[24] E. O. Lachman, M. Mogi, J. Sarkar, A. Uri, K. Bagani, Y. Anahory, Y. Maysoedov, M. E. Huber, A. Tsukazaki, M. Kawasaki, Y. Tokura, and E. Zeldov, arXiv:1710.06446.
[25] S. Grauer, K. M. Fijalkowski, S. Schreyeck, M. Winnerlein, K. Brunner, R. Thomale, C. Gould, and L. W. Molenkamp, Phys. Rev. Lett. **118**, 246801 (2017).
[26] M. Mogi, R. Yoshimi, A. Tsukazaki, K. Yasuda, Y. Kozuka, K. S. Takahashi, M. Kawasaki, and Y. Tokura, Appl. Phys. Lett. **107**, 182401 (2015).
[27] K. Yasuda, R. Wakatsuki, T. Morimoto, R. Yoshimi, A. Tsukazaki, K. S. Takahashi, M. Ezawa, M. Kawasaki, N. Nagaosa, and Y. Tokura, Nat. Phys. **12**, 555 (2016).
[28] Y. Zhang, K. He, C. Z. Chang, C. L. Song, L. L. Wang, X. Chen, J. F. Jia, Z. Fang, X. Dai, W. Y. Shan, S. Q. Shen, Q. Niu, X. L. Qi, S. C. Zhang, X. C. Ma, and Q. K. Xue, Nat. Phys. **6**, 584 (2010).
[29] Y. P. Jiang, Y. L. Wang, M. Chen, Z. Li, C. L. Song, K. He, L. L. Wang, X. Chen, X. C. Ma, and Q. K. Xue, Phys. Rev. Lett. **108**, 016401 (2012).
[30] T. Zhang, J. Ha, N. Levy, Y. Kuk, and J. Stroscio, Phys. Rev. Lett. **111**, 056803 (2013).
[31] See Supplemental Material at http://link.aps.org/supplemental/10.1103/PhysRevLett.120.056801 for MBE growth and characterizations of the sandwich heterostructures, device fabrications, additional transport results and MFM images, and other supporting data, which includes Refs. [32–35].
[32] J. S. Zhang, C. Z. Chang, Z. C. Zhang, J. Wen, X. Feng, K. Li, M. H. Liu, K. He, L. L. Wang, X. Chen, Q. K. Xue, X. C. Ma, and Y. Y. Wang, Nat. Commun. **2**, 574 (2011).
[33] C. Z. Chang, J. S. Zhang, M. H. Liu, Z. C. Zhang, X. Feng, K. Li, L. L. Wang, X. Chen, X. Dai, Z. Fang, X. L. Qi, S. C. Zhang, Y. Y. Wang, K. He, X. C. Ma, and Q. K. Xue, Adv. Mater. **25**, 1065 (2013).
[34] A. J. Bestwick, E. J. Fox, X. F. Kou, L. Pan, K. L. Wang, and D. Goldhaber-Gordon, Phys. Rev. Lett. **114**, 187201 (2015).
[35] C. Z. Chang, W. W. Zhao, D. Y. Kim, P. Wei, J. K. Jain, C. X. Liu, M. H. W. Chan, and J. S. Moodera, Phys. Rev. Lett. **115**, 057206 (2015).
[36] X. F. Kou, L. Pan, J. Wang, Y. B. Fan, E. S. Choi, W. L. Lee, T. X. Nie, K. Murata, Q. M. Shao, S. C. Zhang, and K. L. Wang, Nat. Commun. **6**, 8474 (2015).
[37] Y. Feng, X. Feng, Y. B. Ou, J. Wang, C. Liu, L. G. Zhang, D. Y. Zhao, G. Y. Jiang, S. C. Zhang, K. He, X. C. Ma, Q. K. Xue, and Y. Y. Wang, Phys. Rev. Lett. **115**, 126801 (2015).
[38] J. Wang, B. Lian, and S. C. Zhang, Phys. Rev. B **89**, 085106 (2014).
[39] P. Walser, M. Hunziker, T. Speck, and M. Landolt, Phys. Rev. B **60**, 4082 (1999).
[40] J. Faure-Vincent, C. Tiusan, C. Bellouard, E. Popova, M. Hehn, F. Montaigne, and A. Schuhl, Phys. Rev. Lett. **89**, 107206 (2002).
[41] Z. C. Zhang, X. Feng, M. H. Guo, K. Li, J. S. Zhang, Y. B. Ou, Y. Feng, L. L. Wang, X. Chen, K. He, X. C. Ma, Q. K. Xue, and Y. Y. Wang, Nat. Commun. **5**, 4915 (2014).
[42] M. Mogi, M. Kawamura, A. Tsukazaki, R. Yoshimi, K. S. Takahashi, M. Kawasaki, and Y. Tokura, Sci. Adv. **3**, eaao1669 (2017).